Room-temperature large magnetoelectricity in a transition metal doped ferroelectric perovskite

Shalini Kumari [1,2,*] Dhiren K. Pradhan [3,4,†] Shi Liu,[5] M. M. Rahaman,[6] Peng Zhou,[7] Kevin M. Roccapriore,[4]
Dillip K. Pradhan [8] Gopalan Srinivasan,[7] Qi Li [1] Ram S. Katiyar [9] Philip D. Rack [3,4] J. F. Scott,[10] and Ashok Kumar[11]

[1]*Department of Physics, The Pennsylvania State University, University Park, Pennsylvania 16802, USA*
[2]*Department of Materials Science and Engineering, The Pennsylvania State University, University Park, Pennsylvania 16802, USA*
[3]*Department of Materials Science & Engineering, University of Tennessee, Knoxville, Tennessee 37996, USA*
[4]*Center for Nanophase Materials Sciences, Oak Ridge National Laboratory, Oak Ridge, Tennessee 37831, USA*
[5]*School of Science, Westlake University, 18 Shilongshan Road, Hangzhou 310024, Zhejiang Province, China*
[6]*Geophysical Laboratory, Carnegie Institution for Science, Washington, DC 20015, USA*
and Department of Materials Science and Engineering, University of Rajshahi, Rajshahi 6205, Bangladesh
[7]*Physics Department, Oakland University, Rochester, Michigan 48309-4401, USA*
[8]*Department of Physics and Astronomy, National Institute of Technology, Rourkela-769008, India*
[9]*Department of Physics and Institute for Functional Nanomaterials, University of Puerto Rico, San Juan, Puerto Rico 00931, USA*
[10]*Department of Chemistry and Department of Physics, University of St. Andrews, St. Andrews KY16 ST, United Kingdom*
[11]*CSIR-National Physical Laboratory, Dr. K. S. Krishnan Marg, New Delhi 110012, India*

There is increasing interest in novel magnetoelectric (ME) materials that exhibit robust ME coupling at room temperature (RT) for advanced memory, energy, spintronics, and other multifunctional device applications, by making use of the ability to control polarization with a magnetic field and/or magnetization via an electric field. Obtaining ME materials with strong ME coupling, understanding the origin, and manipulating its processing along with composition to realize large ME coefficients at RT constitute an important step in multiferroic research. To address this, we have investigated the multiferroic and ME properties of Ni-doped $Pb(Zr_{0.20}Ti_{0.80})O_3$ (PZT). We find that the ferroelectric ($T_C \sim 700$ K) and weak ferromagnetic (~ 602 K) phase transitions of Ni-doped PZT are well above room temperature (RT), leading to a strong ME coupling coefficient ($\alpha_{E,31}$) of $11.7 \, \mathrm{mV \, cm^{-1} \, Oe^{-1}}$ ($H_{ac} = 1$ Oe and $f = 1$ kHz). While x-ray diffraction suggests a single-phase material, high-resolution transmission electron microscopy reveals regions with and without Ni present; thus magnetoelectric coupling between two phases is possible. First-principles calculations suggest the $(Ni_{Pb})^{\times}$ defect is likely to be responsible for the experimental observed magnetism and ME coupling in Ni-doped PZT. We further demonstrate that Ni-doped PZT exhibits low loss tangent, low leakage current, large saturation polarization, and weak ferromagnetism. Ultimately, our work demonstrates that Ni-doped PZT is a cost-effective RT multiferroic with strong ME coupling.

I. INTRODUCTION

Magnetoelectric-multiferroic (ME-MF) materials exhibiting the coexistence of ferroelectric (FE) and ferromagnetic (FM) orderings in a single-phase and permitting the switching and control of the magnetization (M) by suitable electric field (E), and electrical polarization (P) via suitable magnetic field (H), have recently drawn enormous interest due to their fascinating physics and have strong potential for memory, spintronics, and various multifunctional device applications [1–5]. Magnetoelectric materials exhibiting robust ME coupling have potential for memory applications and device miniaturization beyond Moore's law [3,5,6]. Due to the intrinsic incompatibility among the magnetic and ferroelectric orderings in oxide perovskites,

very few single-phase multiferroic oxides exist in nature, such as $BiFeO_3$, $GaFeO_3$, $Pb(Fe_{0.5}Nb_{0.5})O_3$, $YMnO_3$, $Pb(Fe_{0.5}Ta_{0.5})O_3$, $ErMnO_3$, $Pb(Fe_{0.67}W_{0.33})O_3$, and $TbMnO_3$ [1,7]. $BiFeO_3$ (BFO) is the most studied room temperature (RT) lead-free, simple, and perovskite structured single-phase multiferroic material having both FE and antiferromagnetic (AFM) critical temperatures above RT [8–10]. For practical device applications, it is still not suitable, because of its high leakage current and lower ME coupling coefficient. Most of the other multiferroic materials exhibit ferroelectric and/or magnetic phase transitions at cryogenic temperatures [9,11,12]. The large difference between the ferroelectric and magnetic ordering temperatures often suggests small ME coupling [11,12]. Realizing strong ME coupling above RT in single-phase materials and understanding its origin is vitally important for practical applications [1,2,11,12].

To realize both magnetic and ferroelectric orderings above RT with large ME coupling, composite structures of strong ferroelectric and magnetic materials have been envisioned and produced [13–19]. But for some specific device

---

*shalinikumari1990@gmail.com
†dhirenkumarp@gmail.com

geometries and applications (such as multiferroic tunnel junctions), single-phase ME materials are necessary because the electrical switching and control of magnetization is remarkably faster in the case of single-phase multiferroics compared to composite ME materials (where it is strain coupled and therefore is limited by the speed of sound) [11,12,20,21]. Understanding the mechanisms and nature of ME coupling is a long-standing research topic in condensed matter physics as it is required for enabling a number of potential devices which make use of controlling electronic order parameters by magnetic field or magnetism via an electric field [1,2,8,11,18]. Manipatruni *et al.* from the Intel research group have fabricated scalable ME spin orbit logic devices that operate by spin-orbit transduction and ME switching [22]. La-doped $BiFeO_3$ was utilized as a single-phase ME material in this device, which exhibits higher switching energy ($\sim$10–30 times), lower switching voltage ($\sim$5 times) and superior logic density ($\sim$5 times) than the present complementary metal-oxide-semiconductor (CMOS) devices [22]. Due to higher leakage current along with lower ME coupling of La-doped $BiFeO_3$, it is still not ideal [9]. Hence, the realization of strong ME coupling at RT through new materials is very promising, which could enable a wide range of ME devices. Thus, we have systematically investigated the multiferroic and magnetoelectric properties of Ni-doped PZT, i.e., $Pb(Zr_{0.20}Ti_{0.0.80})_{0.70}Ni_{0.30}O_3$ or $Pb(Zr_{0.14}Ti_{0.56}Ni_{0.30})O_3$, hereafter referred to as PZTNi throughout the paper. $Pb(Zr_{0.20}Ti_{0.80})O_3$ is one of the best ferroelectric materials with a ferroelectric $T_C \sim 720$ K with high dielectric permittivity and high piezoelectric coefficient along with low dielectric loss tangent at RT, whereas Ni is a transition metal usually having ferromagnetic behavior and is relatively cheap [12,23–27]. PZTNi thin films show large polarization and good photovoltaic properties [23,24]. Here we have systematically investigated the structural, ferroelectric, magnetic, and ME coupling properties of PZTNi ceramics at RT. Interestingly, we also found similar ferroelectric and magnetic ordering temperatures. We find that this material shows strong ME coupling with both magnetic and ferroelectric phase transitions well above RT. As we will show, while x-ray diffraction results suggest a single-phase material, transmission electron microscopy reveals Ni-rich and Ni-deficient regions; thus magnetoelectric coupling between two phases could be operative.

II. EXPERIMENTAL DETAILS

PZTNi polycrystalline ceramic powders were prepared via the high-temperature solid-state reaction synthesis technique from the stoichiometric mixing of high-purity ($> 99.99\%$) ZrO_2, PbO, NiO, and TiO_2 precursors from Alfa Aesar. Planetary mechanical ball milling of the precursors with required stoichiometric amounts was carried out with zirconium balls in a methanol media. These powders were calcined in air at an optimized temperature of 1373 K for 10 h, using a high-temperature Carbolite furnace (Model: HTF1700) with a controlled heating rate of 5 K/min. The long-time high energy along with high-temperature ball milling process significantly enhances the chemical processing and desired phase material formation. The phase-pure PZTNi powders were pressed to cylindrical pellets having a diameter of $\sim$13 mm, utilizing a hydraulic press under an isostatic pressure of $\sim 5 \times 10^6$ Nm^{-2}.

The phase formation along with the phase purity of the sintered PZTNi pellets was examined by x-ray diffraction (Rigaku Ultima III) using a Cu $K\alpha$ radiation source at 40 kV and 40 mA with a slow scan rate of $0.2°$/min. Later the Rietveld refinement was performed using FULLPROF SUITE software. Field emission scanning electron microscopy (FESEM) and elemental mapping images were recorded utilizing a Zeiss Auriga FESEM equipped with an Oxford Instruments X-Max 80 (SDD) energy-dispersive X-ray spectroscopy (EDS) system. Scanning transmission electron microscopy (STEM) measurements were carried out using a fifth order aberration-corrected NION UltraSTEM 200, which is operated at an accelerating voltage of 200 kV and convergence semiangle of 30 mrad. Electron energy loss (EEL) spectra were acquired at core-loss energies at numerous probe positions to generate a three-dimensional data cube, or so-called spectrum image, which permits visualization of selected energy losses in space. In this way, we observe the spatial distribution of different atomic species and their chemical state, e.g., Ti and Ni. Note that high-angle annular dark field (HAADF) images were recorded in parallel to the EELS acquisition. The existence of all elements and valence states of the synthesized pellets were investigated via x-ray fluorescence spectroscopy (XRF) and high-resolution x-ray photoelectron spectroscopy (XPS) studies, respectively. Structural analyses and phase transitions studies were done by performing temperature dependence of Raman spectroscopy, with a T64000 spectrometer which is operated in backscattering configuration along with subtractive mode. Continuous power, 8 mW, was focused to a small spot size of $\sim 2\ \mu m^2$ from an Innova Coherent argon ion laser having a wavelength of 5145 Å. A charge-coupled device (CCD) cooled with liquid nitrogen was utilized to collect the low- and high-temperature Raman scattering signal through an $80\times$ objective under vacuum in the temperature range of 83–900 K in steps of 25 K using Linkam temperature controllers (TP93 and TMS94) along with a liquid nitrogen pump cooling module. Both the flat surfaces of the phase-pure sintered pellets were polished using fine emery papers, and then electrodes (top and bottom) were prepared with highly pure silver paint. The painted pellets are then heated at $\sim$373 K for 2 h in air atmosphere for better adhesion and conduction. The dielectric parameters were measured utilizing an HP4294A impedance analyzer under high vacuum (10^{-6} Torr). Thermal control was maintained using a variable temperature microprobe station (MMR Technologies, Inc.) equipped with a fine programmable temperature controller (K-20 of MMR) in the range of 80–700 K. Ferroelectric hysteresis behavior was measured at RT utilizing a hysteresis loop tracer (Radiant: RT 6000 HVS) after electrical poling of the sample at a voltage of $\sim$1200 V for 4 h using a dc power supply (Trek: 677A). Magnetic properties [M as a function of temperature (T) and H] of the PZTNi samples were performed using a physical properties measurement system (PPMS), the DynaCool system from Quantum Design, capable of measuring the temperature from 300 to 800 K. The dynamic magnetoelectric measurements were carried out at RT utilizing a homemade ME coupling setup, having a magnet

with varying magnetic field of up to ± 1500 Oe and a lock-in amplifier along with a Helmholtz coil.

A. Computational methods

All density functional theory calculations are carried out using QUANTUM ESPRESSO with PBEsol density functional approximation and $2 \times 2 \times 2$ Monkhorst-Pack sampling [28]. The ultrasoft pseudopotentials were used from the Garrity *et al.* high-throughput pseudopotential set [29] and a plane-wave cutoff of 50 Ry along with a charge density cutoff of 250 Ry. To better describe the *d* states of Ni, we used the DFT + *U* method where a Hubbard-like *U* term is introduced [30]. The value of *U* is determined by the self-consistent linear-response method implemented in QUANTUM ESPRESSO [31]. Specifically, we first relax Ni-doped $PbTiO_3$ with lattice constants fixed to experimental values with PBEsol; then we carry out the linear-response approach to estimate the *U* value. For $(Ni_{Pb})^{\times}$, the calculated *U* value is 7.0 eV, and for both $(Ni_{Ti})^{\times}$ and $[Ni''_{Ti} - V^{\cdot\cdot}_O)^x]$, the *U* value is 9.3 eV. An energy convergence threshold of 1.0×10^{-4} Ry and a force convergence threshold of 1.0×10^{-3} Ry/bohr and a Marzari-Vanderbilt smearing of 1 mRy are used to fully relax the atomic positions.

III. RESULTS AND DISCUSSION

A. X-ray diffraction

The XRD patterns of PZTNi samples were recorded in the 2θ range of $20° - 60°$ for structural analysis of the material. The presence of sharp diffraction peaks indicates good homogeneity and crystallization of the samples. A close examination of the XRD patterns suggests a single-phase with no lead-deficient pyrochlore phases. The Rietveld refinement of the XRD patterns was carried out to obtain detailed structural information about the material [32]. We have taken the polar space group *P4mm* of tetragonal crystal structure for the refinement. In the unit cell of PZTNi with the *P4mm* space group, Pb occupies the $1a$ (0, 0, *z*) site, $Zr^{4+}/Ti^{4+}/Ni^{2+}$ occupies the $1b$ site (0.5, 0.5, *z*), oxygen O1 the $1b$ site (0.5, 0.5, *z*), and oxygen O2 the $2c$ site (0.5, 0, *z*). We have used the Thompson-Cox-Hastings pseudo-Voigt asymmetry function to describe the peak profile function, whereas a linear interpolation technique was used to describe the background. The adjustable parameters, such as zero correction, half-width parameter (*U*, *V*, *W*), scale factor, lattice parameter, background, and position coordinates have been optimized throughout the refinement. The occupancy parameters of the ions were fixed during the refinement process. The Rietveld refinement pattern of PZTNi is shown in Fig. 1, where the experimental data are shown as circles and the simulated data are displayed as the solid line. The difference between experimental and the simulated data is shown at the bottom of the plot, along with the vertical lines which indicate positions of the Bragg reflections. A good match between the experimental and simulated data is obtained with the goodness of fit parameter χ^2 value 2.18. The observed lattice parameters are $a = b = 3.9639$ Å(1), $c = 4.1279(1)$ Å with a tetragonality (*c/a*) ratio of 1.041 which corresponds to the normal ferroelectric behavior. We observed a slight decrease of *c/a* ratio
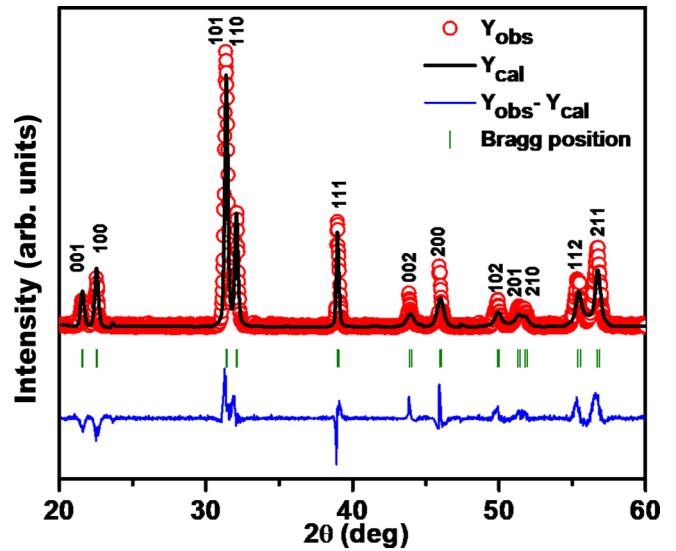

FIG. 1. The Rietveld refined XRD patterns of PZTNi ceramics using FULLPROF SUITE software.

of PZTNi compared to pure $Pb(Zr_{0.20}Ti_{0.80})O_3$, which has lattice parameters of $a = b = 3.954$ Å, $c = 4.132$ Å with a *c/a* ratio of 1.045 [33]. The decrease of the tetragonality ratio might be due to the pinning of the ferroelectric domain by Ni. Cr (Cr_2O_3) doping at 30 % in $Pb_{0.94}Sr_{0.06}(Zr_{0.53}Ti_{0.47})O_3$ reduces the *c/a* ratio from 1.023 to 1.021, whereas 30 % of Mn (MnO_2) doping in $Pb_{0.94}Sr_{0.06}(Zr_{0.53}Ti_{0.47})O_3$ reduces the *c/a* ratio from 1.023 to 1.017 [34]. The observation of tetragonality in PZTNi is consistent with the other Ti-rich systems of PZT with high tetragonality [12,35]. From the observed lattice parameters we can conclude that there is no significant change in the basic crystal structure of PZT with substitution of 30 % Ni^{2+}. As is discussed below, some nanoscale phase separation is observed in the scanning transmission electron microscope, suggesting two phases, with albeit similar structure. Thus, while the XRD suggests a single-phase, one cannot rule out size effects and poor crystallinity in the minor phase component may wash out the second phase Bragg peaks.

B. Microscopic studies

We investigated the microstructural surface morphology and performed elemental mapping of PZTNi using FESEM (Supplemental Material, S1) [36]. It is observed that all the elements are uniformly distributed in the large area of $\sim$25 $\times$ 25 μm^2. Ni (green) is distributed homogeneously throughout and no clustering is observed within the resolution limit of the image. The distribution of Ni is also studied in a single grain of PZTNi, which also appears homogeneously distributed.

High-resolution scanning transmission electron microscopy (STEM) measurements did observe some nanoscale phase separation with Ni and Ti segregation (see the Supplemental Material, S2) [36]. The combined XRD, SEM, and STEM suggest that while there are some regions of nanoscale segregation the structures are similar and not distinguishable in the XRD.
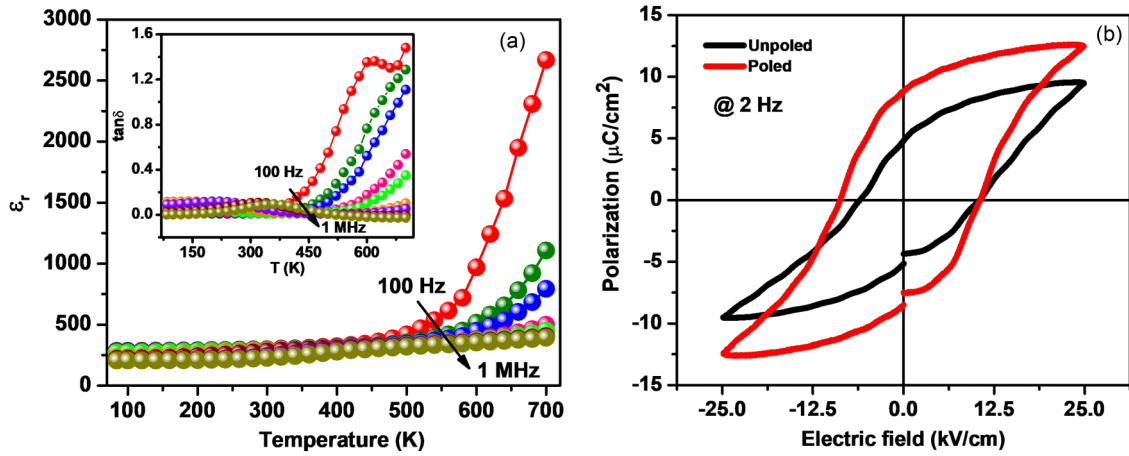
FIG. 2. (a) Temperature dependence of relative dielectric permittivity of PZTNi ceramics at different frequencies; the inset shows respective temperature dependence of tanδ. (b) Ferroelectric (*P-E*) hysteresis loops of poled and unpoled PZTNi at RT.

C. Calorimetric, dielectric, ferroelectric, and leakage current properties

To get insight into the FE ordering temperature and phase transition behavior, temperature dependence of dielectric permittivity (ε_r) measurements were carried out over a large range of frequencies [Fig. 2(a)]. The dielectric permittivity (ε_r) is found to decrease with rise in frequency for PZTNi, which is a characteristic of polar dielectrics. The dielectric permittivity increases slowly with increasing temperature up to 550 K and then increases rapidly up to 700 K. We could not probe the ferroelectric-paraelectric phase transition temperature (T_C) due to experimental limitation, however, from this figure. it is clear that the ferroelectric T_C of PZTNi lies at or above 700 K. We have also probed the ferroelectric phase transition of PZTNi by Raman spectroscopy measurements that are discussed in the following section. The inset of Fig. 2(a) shows the loss tangent (tanδ) of PZTNi as a function of temperature at different frequencies. The tanδ increases with increasing temperature, and the increase is more prominent at higher temperature; this might be due to the existence of space charge polarization along with interfacial polarization across the Ag/PZTNi interface [12,37]. The RT loss tangent is found to be very low (0.009 at 1 kHz), which makes this material a suitable candidate for device applications.

To probe the ferroelectric phase transition further, we have performed differential scanning calorimetry (DSC) studies from RT to 1000 K (see the Supplemental Material, S3(a) [36]). We observed a sharp endothermic peak ~705 (± 10) K. The presence of the endothermic anomaly in the DSC thermogram suggests that the ferroelectric-paraelectric phase transition occurs around 705 (±10) K. The occurrence of the endothermic transition is corroborated by the Raman studies below.

The existence of ferroelectricity in PZTNi ceramics is examined by measuring the electric field (*E*) dependent electrical polarization (*P*) hysteresis loops at RT for poled and unpoled samples at a frequency of 2 Hz [Fig. 2(b)]. The ferroelectric hysteresis measurements were performed after electrical poling of the sintered pellet at 12 kV/cm for 6 h. Both the unpoled and poled samples exhibit well satu-

rated square hysteretic behavior with saturation polarization (P_s) 9.5, 12.5 (±0.5) μC/cm^2, remnant polarization (P_r) 5.1, 8.7 (±0.5) μC/cm^2, and coercive field (H_c) 8.25 and 9.5, (±0.5) kV/cm, respectively, at a maximum applied electric field of 25 kV/cm. The P_s, P_r, and H_c values of poled samples are found to be higher than the unpoled samples.

The leakage current density of PZTNi ceramic was observed to be 1.08×10^{-9} A/cm^2 at very small applied electric field but 4.5×10^{-7} A/cm^2 at the maximum applied electric field of ~6 kV/cm (see the Supplemental Material, S3(b) [36]). The leakage current observed in our sample is found to be lower than BiFeO$_3$ [38]. As the RT leakage current and loss tangent of PZTNi are both low, therefore good ferroelectric behavior has been observed and strong ME coupling is expected.

D. Raman spectroscopic studies

Temperature dependent Raman scattering spectra have been investigated to probe the ferroelectric phase transition and to understand the phonon dynamics of PZTNi ceramics [39,40]. Here, the reduced intensity $I^r(\omega)$ was computed from the Stokes component of the observed Raman scattering intensity $I(\omega)$ using the equation given below to avoid the effect of Bose-Einstein phonon population [39,40]:

$$I^r(\omega) = \frac{I(\omega)}{\omega[n(\omega)+1]}, \qquad (1)$$

where $n(\omega) = \frac{1}{\exp(\hbar\omega/k_B T)-1}$ is the Bose-Einstein population factor, where $\hbar$ and k_B are the Dirac and Boltzmann constants, respectively. The temperature dependent reduced Raman spectra of the PZTNi ceramic is shown in Fig. 3(a). To understand the phonon dynamics in detail and to clarify the ferroelectric phase transition that was not observed in the dielectric spectroscopy due to experimental limitations, we fit all the reduced spectra in the frequency range of 12–400 cm^{-1} with the combination of a Lorentzian central peak (CP) and a DHO (damped harmonic oscillator) model using the equation
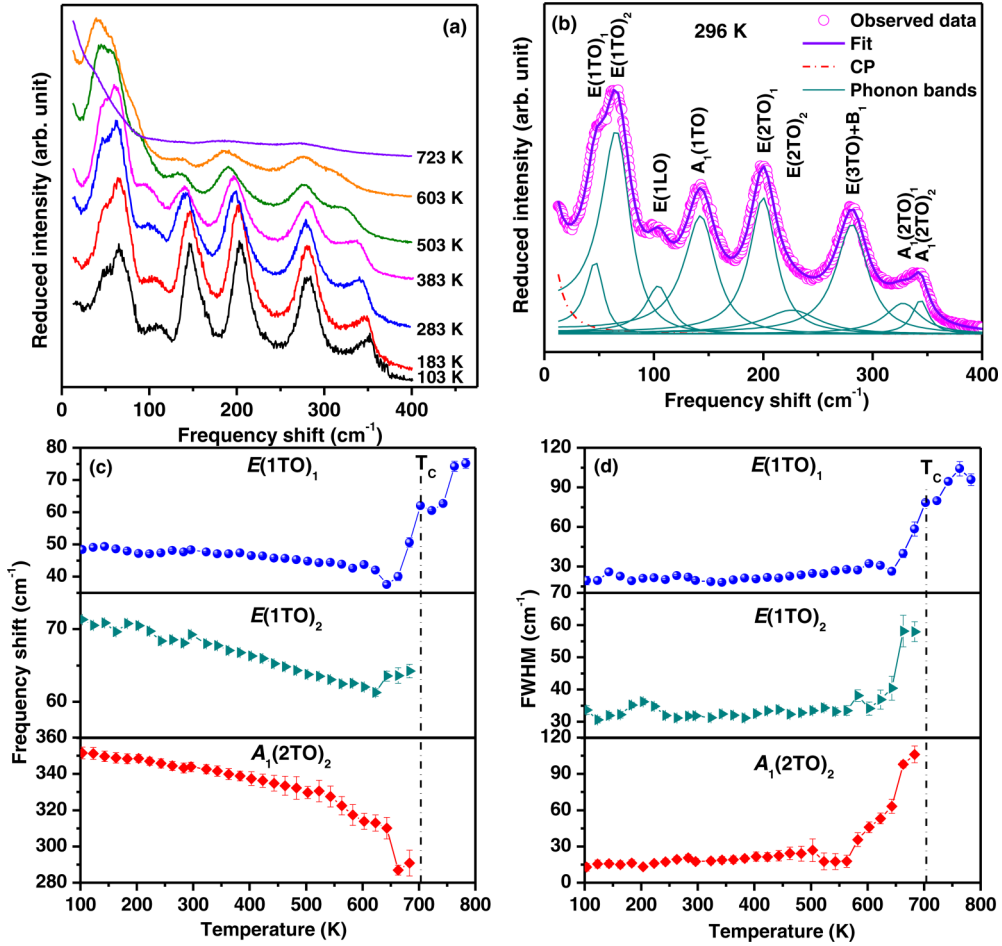
FIG. 3. (a) The temperature dependence of reduced Raman spectra of PZTNi at selected temperatures. The example of a fit of the Raman spectrum at 296 K using Eq. (2) is shown in (b). (c) The temperature dependence of the frequency shift of first order modes at around 48, 68, and 344 cm^{-1} of the PZTNi ceramic. (d) The FWHM of the modes at about 48, 68, and 344 cm^{-1} of the PZTNi ceramic as a function of temperature.

given below [25,39–42].

$$I^r(\omega) = \frac{2A_{CP}}{\pi} \frac{\Gamma_{CP}}{4\omega^2 + \Gamma_{CP}^2} + \sum_i \frac{A_i \Gamma_i \omega_i^2}{\left(\omega^2 - \omega_i^2\right)^2 + \omega^2 \Gamma_i^2}, \quad (2)$$

where Γ_{CP} and A_{CP} are the full width at half maximum (FWHM) and intensity of the CP respectively. Γ_i, ω_i, and A_i are the damping constants, frequency, and intensity of the ith Raman active optical mode, respectively. Figure 3(b) shows the example of a fit of Raman spectrum using Eq. (2). The detailed assignment of Raman modes of the PZT were reported elsewhere [29,42,43]. At 296 K, the frequencies of several Raman modes of the PZTNi have been found at 48, 68, 104, 145, 197, 206, 280, 329, and 344 cm^{-1} as shown in Fig. 3(b). In the cubic phase of PbTiO$_3$ and in the cubic phase of PbTiO$_3$, the optic modes transform as the $3T_{1u} + T_{2u}$ irreducible presentations of the space group $Pm\bar{3}m$. The three triply degenerate T_{1u} modes are infrared (IR) active, whereas the triply degenerate T_{2u} mode is both IR and Raman inactive (often called a "silent mode"). In the tetragonal ferroelectric phase with $P4mm$ symmetry, all the phonons become Raman active. Each of the T_{1u} modes splits into modes of symmetry

$A_1 + E$, and the T_{2u} mode splits into modes of $B_1 + E$ symmetry in the tetragonal phase.

Here we are mainly concerned about the low-frequency Raman modes of the PZTNi ceramic. In polycrystalline ceramics, direct assignments of mode symmetries are not possible from the Raman spectra measurements. Hence, the assignments of mode symmetries in PZTNi were carried out by following the mode assignments of PZT35 single crystals [42]. It is seen that the Raman spectra of the PZTNi consist of mainly $E(1TO)$ (~ 60 cm^{-1}) (~ 60 cm^{-1}), $E(1LO)$ (~ 104 cm^{-1}), $A_1(1TO)$ (~ 145 cm^{-1}), $E(2TO)$ (~ 200 cm^{-1}), $E(3TO) + B_1$ doublet (~ 280 cm^{-1}), and $A_1(2TO)$ (~ 345 cm^{-1}) modes in the frequency range of 12–400 cm^{-1} [Fig. 3(b)]. It is also important to note that the $E(1TO)$, $E(2TO)$, and $A_1(2TO)$ modes each split into two modes denoted as $E(1TO)_1$ (48 cm^{-1}) and $E(1TO)_2$ (68 cm^{-1}), and $E(2TO)_1$ (197 cm^{-1}) and $E(2TO)_2$ (206 cm^{-1}), and $A_1(2TO)_1$ (~ 329 cm^{-1}) and $A_1(2TO)_2$ (~ 344 cm^{-1}), respectively [Fig. 3(b)]. The splitting of the transverse E and A modes can be due to the different local order regions in PZTNi ceramic (e.g., slight orthorhombic symmetry) [29]. Another possibility for the splitting of E and A modes might be due to the partial occupancy of small percentage of Ni at the A

site in Ni-rich PZT. The effect of partial occupancy of the Ni at both the A and B sites is discussed in the Theory section. In the low-frequency region, the following variations were noticed in the spectra upon heating: (i) most of the intense modes shift toward lower frequency; (ii) most of the modes broaden; and (iii) mode intensities diminish and disappear completely for phonon branches at around 68, 104, 222, 329, and 344 cm^{-1} as the temperature approaches at the ferroelectric to paraelectric phase transition temperature (T_C) (Fig. 3). These observations can be suitably described by anharmonic lattice effects and thermal broadening, along with thermal disorder. In addition, the modification of bond length between oxygen and the cations (thermal expansion) might decrease vibrational frequencies with the increase of temperature. All the Raman modes show changes in their line shapes, but for the clarity we present only the frequency and FWHM of $E(1TO)_1$, $E(1TO)_2$, and $A_1(2TO)_2$ modes.

The temperature dependent frequency and FWHM of these modes are plotted in Figs. 3(c) and 3(d), respectively. Note that the frequency of the $E(1TO)_2$ and $A_1(2TO)_2$ modes shifts remarkably toward lower frequency with increasing of temperature and vanishes above $T_C = 703 \pm 10$ K, while the frequency of the $E(1TO)_1$ mode shows slight softening and a clear anomaly at around T_C. The FWHM of Raman modes exhibits a clear anomaly at about T_C as well [Fig. 3(d)]. The complete disappearance and the anomalous change of Raman modes at around T_C were reported in different types of materials such as ferroelectric and multiferroic materials [16,39,40]. It is also significant that the FWHM of these modes increases gradually with increasing of temperature as the temperature approaches T_C, implying some order-disorder type of the ferroelectric phase transition of the PZTNi ceramic. In inelastic light scattering the ferroelectric soft mode is a general property of a crystal/ceramic which undergoes a displacive phase transition, whereas the CP is a common feature of the order-disorder phase transition. Fontana *et al.* reported the coexistence of the displacive and the order-disorder phase transition in KNbO$_3$ by the observation of the soft mode and the CP using Raman scattering [44]. In the present study, the soft mode of the PZTNi ceramic was not observed. However, the prominent CP was clearly observed in the vicinity of the T_C of the PZTNi ceramic [Fig. 3(a)]. Hence, the occurrence of the broad CP can be the clear evidence of the order-disorder nature of the ferroelectric phase transition of the PZTNi ceramic. According to the Raman selection rules, first-order Raman modes are prohibited in the paraelectric cubic phase having $Pm\bar{3}m$ symmetry. However, these first-order modes still exist in the paraelectric cubic phase, as shown in Fig. 3(c). Therefore, the existence of the first order mode in the paraelectric phase demonstrates the local noncubic symmetry breaking. The local symmetry breaking could be due to polar distortions/fluctuations and/or octahedral tilting [16,39,40,45]. The disappearance of some Raman modes above a certain temperature shows that either the sample has decomposed and become amorphous, or it has transformed to its cubic phase via a structural phase transition. We tested the probability of the former case by capturing the Raman spectra by cooling it to RT and observed that all the modes distinctly reappear, which clearly rules out the probability of decomposition of the material and indicated that the

PZTNi samples actually transformed to a cubic phase above transition temperature (T_C) [16].

E. Magnetic properties

We measured the dc magnetization of the PZTNi sample as a function of temperature (*M-T*) in the temperature range of 300–800 K and dc applied magnetic field (*M-H*) (Fig. 4). All the *M-T* and *M-H* measurements were performed in the in-plane (*H* parallel to the surface of the sample) configuration. Temperature dependence of zero field cooled (ZFC) and field-cooled (FC) magnetic measurements were carried out under an external dc field of 100 Oe [Fig. 4(a)]. We found a slight bifurcation in the ZFC-FC curve, which indicates that PZTNi has less magnetic frustration in the system, since a ZFC-FC bifurcation indicates the presence of a magnetic instability [23]. The magnetization decreases slowly up to 550 K and then decreases suddenly with the increase of temperature and is almost constant above ~610 K but does not vanish completely. The estimated magnetic transition temperature for PZTNi is observed around 602 ($\pm$10) K with a relaxor paramagnetic background.

The magnetic properties of PZTNi were further investigated by measuring the magnetization as a function of applied dc magnetic field (*M-H* loops) at different temperatures [Fig. 4(b)]. The *M-H* loop measured at RT shows weak ferromagnetic behavior having remanent magnetization (M_r) of ~0.002 emu/g and coercive field (H_c) of 112 ($\pm$4) Oe. With increasing temperature, M_s and M_r are found to decrease, without the complete saturation of magnetization. The *M-H* loop of PZTNi ceramics recorded at 635 K which is above the phase transition (~602 K) shows paramagnetic behavior [inset of Fig. 4(b)]. From both figures it is clear that PZTNi indeed undergoes a ferromagnetic to paramagnetic transition. The observed magnetic behavior in PZTNi is assumed to be because of the substitution of Ni^{2+} into the PZT host lattice. Similar phenomena have also been observed in other transition metal (Fe and Mn) doped PbTiO$_3$ perovskites [46,47].

F. Magnetoelectric coupling

The existence of coupling between the electrical and magnetic order parameters in PZTNi ceramics was investigated by measuring magnetoelectric voltage coefficients (α_{ME}) via a dynamic method at low frequencies [48]. The sample was initially poled electrically at ~6 kV/cm at RT for 4 h. Here we measured the change in electric field by an alternating magnetic field applied to the sample surface. In the ME measurement setup, the sample was subjected to external bias field *H* by using an electromagnet whereas an ac magnetic field δH (1 Oe) was produced by a pair of Helmholtz coils and the lock-in detection unit was used to measure the ME voltage (δV) generated across the thickness of the sample. The measurements were carried out for the in-plane mode for δH and *H* parallel to each other and to the sample plane (i.e., along the direction 1) and perpendicular to the δE along direction 3 (denoted as transverse orientation α_{31}). The transverse ME voltage coefficient ($\alpha_{E,31}$) was measured as a function of static magnetic field ($H = 0 \pm 3000$ Oe) with ac field (δH) varying from 1 to 10 Oe with frequencies ranging from 30 to 100 Hz and at RT (Fig. 5). Figures 5(a) and 5(b) depict
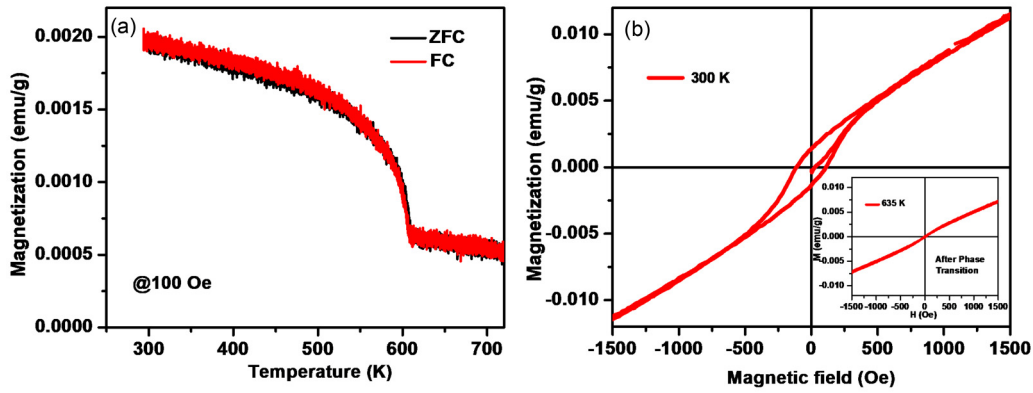
FIG. 4. (a) ZFC and FC plots of PZTNi ceramics at 1000 Oe. Magnetic (*M-H*) hysteresis loops of PZTNi at (b) 300 K, (c) 500 K, and (d) 900 K, respectively.

the magnetic field dependence of $\alpha_{E,31}$ at some selected ac magnetic field (H_{ac}) at different frequencies (30 Hz and 1 kHz). The magnitude of $\alpha_{E,31}$ is almost constant with increasing H. With increasing H_{ac} the magnitude of $\alpha_{E,31}$ decreases. PZTNi exhibits an $\alpha_{E,31} \sim 1.25$ mV cm^{-1} Oe^{-1} at $H_{ac} = 1$ Oe [Fig. 5(a)] and increases to ~ 11.6 mV cm^{-1} Oe^{-1} [Fig. 5(b)] with increase of frequency from 30 Hz to 1 kHz. The ME coupling coefficient of PZTNi is compared with other multiferroic materials (see Table I) [12,49–53]. The observed strong ME coupling in PZTNi may arise because this system exhibits large polarization and weak ferromagnetism and perhaps also due to the close proximity between the ferroelectric and magnetic ordering temperatures ($T_{C(FE)} \sim 700$ K and $T_{C(Magnetic)} \sim 602$ K). The existence of strong ME coupling has been theoretically proposed and experimentally observed in materials that exhibit similar ferroelectric and magnetic ordering temperatures. Observation of strong ME coupling in PZTNi might be due to the local sublattice interactions among the spin moments and the disordered ferroelectric dipole moment [1,2,5]. The presence of strong RT ME coupling makes it promising material for memory, spintronics, and other multifunctional device applications.

G. Theory

A bond magnetic polaron model is proposed to explain the magnetization in transition metal doped ferroelectrics [54]. It was suggested that in Ni-doped PZT ceramics, some bound electrons arise from the oxygen vacancies (V_O^{2-}), which are created to maintain the charge neutrality, and with the oxygen loss during the synthesis. Here, the Ni^{2+} ions and the localized electrons might form bound magnetic polarons. The bound electron occupies a Bohr orbit and, as a bound polaron, it mediates the ferromagnetic (FM) ordering of Ni^{2+} ions within this orbital volume. A FM exchange interaction between the magnetic Ni^{2+} ions and spin-polarized electrons trapped at the oxygen vacancy [Ni^{2+}–(V_O^{2-})–Ni^{2+} groups] may occur [34]. However, this model has never been convincingly demonstrated quantum mechanically.

We carried out first- principles density functional theory (DFT) calculations to understand the origin of magnetism in Ni-doped PZT. Given the chemical similarity between PZT and PbTiO$_3$, we consider Ni-doped PbTiO$_3$ as a model system for DFT investigations where a $2 \times 2 \times 2$ supercell is used. We performed a systematic investigation by considering both point defects and dipolar defects. Various configurations, each containing two Ni dopants so as to study the possible spin-spin coupling effect, were constructed in the following ways: (1) Substitute two Ti cations with Ni dopants isovalently leading to two point defects (Ni$_{Ti}$)$^{\times}$ and a nominal valence state of Ni of $+4$; (2) substitute two Pb cations with Ni dopants leading to charge neutral defects (Ni$_{Pb}$)$^{\times}$ and a charge state of Ni of $+2$; (3) substitute one Ti and one Pb
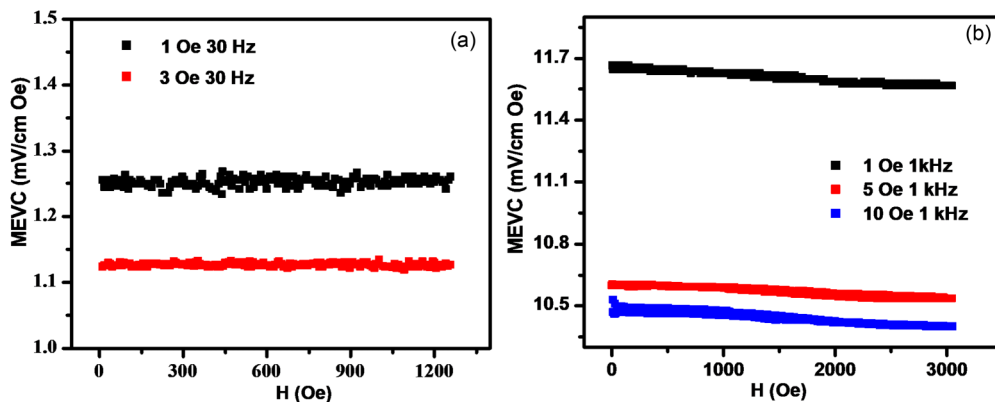

FIG. 5. Magnetoelectric coupling coefficients (a) as a function of an externally applied magnetic field (a) at H_{ac} of 1 and 3 Oe at a frequency of 30 Hz; (b) at H_{ac} of 1, 5, and 10 Oe at a frequency of 1 kHz of PZTNi at RT.

TABLE I. The comparison of ME coupling coefficient of PZTNi with other multiferroic materials.

Materials	ME coupling	H_{ac} and frequency	Reference
$Pb(Zr_{0.20}Ti_{0.80})_{0.70}Ni_{0.30}O_3$	$\alpha_{E,31} = 11.6 \, mV \, cm^{-1} \, Oe^{-1}$	1 Oe and 1 kHz	This work
$Bi_{0.68}Pb_{0.32}Fe_{0.655}Mn_{0.025}Ti_{0.32}O_3$	$\alpha_{E,31} = 0.5 \, mV \, cm^{-1} \, Oe^{-1}$	10 Oe and 100 kHz	[47]
$BiFeO_3$	$\alpha_{E,31} = 0.28 \, mV \, cm^{-1} \, Oe^{-1}$	0.19 kOe and 7 kHz	[44]
$Bi_{0.7}Sr_{0.3}FeO_3$	$\alpha_{E,31} = 0.37 \, mV \, cm^{-1} \, Oe^{-1}$	0.19 kOe and 7 kHz	[44]
$Pb(Zr_{0.20}Ti_{0.80})_{0.70}Pd_{0.30}O_{3-\delta}$	$\alpha_{E,31} = 0.36 \, mV \, cm^{-1} \, Oe^{-1}$	1 Oe and 100 Hz	[12]
$(Bi_{0.95}Nd_{0.05})(Fe_{0.97}Mn_{0.03})O_3$	$\alpha_{E,31} = 0.124 \, mV \, cm^{-1} \, Oe^{-1}$	600 Oe and 1 kHz	[45]
$Bi_{0.9}In_{0.1}Fe_{0.95}Ti_{0.05}O_3$	$\alpha_{E,31} = 4.8 \, mV \, cm^{-1} \, Oe^{-1}$		[45]
$(BiFeO_3)_x$-$(BaTiO_3)_{1-x}$	$\alpha_{E,31} = 0.38 \, mV \, cm^{-1} \, Oe^{-1}$		[45]
$Sr_3Co_2Fe_{24}O_{41}$	$\alpha_{E,31} = 15 \, mV \, cm^{-1} \, Oe^{-1}$	2 Oe and 1 kHz	[48]

with Ni atoms, respectively, resulting in a $Ni^{2+} - Ni^{4+}$ pair; (4) replace Ti with Ni coupled with a nearby oxygen vacancy, resulting in a dipolar defect $[(Ni''_{Ti} - V^{··}_O)^\times]$ if assuming Ni^{2+} or a $Ni^\times_{Ti}V^\times_O$ pair for isovalent substitution; (5) replace Pb with Ni coupled with a neighboring Pb vacancy, creating a dipolar defect $[(Ni^{··}_{Pb} - V''_{Pb})^\times]$ assuming Ni^{2+} or a $Ni^\times_{Pb}$–$V^\times_{Pb}$ pair for isovalent substitution. The lattice constants are fixed to the observed experimental values and the atomic positions are fully rselaxed. Our computational exploration covered a broad range of defect types and oxidation states of Ni. From the XPS spectra of PZTNi, we observed that Ni exists in the +2 valence state (see the Supplemental Material, S4) [36].

We compared the energetics of the (ferro)magnetic, antiferromagnetic, and nonmagnetic states for all possible configurations (see details in the Supplemental Material [36]) and found surprisingly that only when the two Ni^{2+} replace two Pb^{2+}, does the Ni-doped PTO adopt a magnetic insulating

ground state. The lowest-energy configuration has two Ni atoms being the nearest neighbors and Ni-Ni aligned mostly along the c direction [Fig. 6(a)]. Figure 6(b) presents the density of states, which reveals a semiconducting behavior with a band gap of 1.86 eV as confirmed by the band structure shown in Fig. 6(d). Interestingly, we find that only one Ni is spin polarized [labeled as Ni1 in Fig. 6(a)] with a local magnetic moment of $1.68 \, \mu_B$ whereas the other Ni atom is not spin polarized with a local magnetic moment close to zero. This can be understood by the crystal field theory. As shown in Fig. 6(a), Ni1 is coordinated by five oxygen atoms (with Ni-O bond length < 3.0 Å), and thus experiences a square pyramidal crystal field. The Ni1 magnetic moment is $1.68 \, \mu_B$, suggesting a high-spin state and an oxidation state of +2. In comparison, Ni2 is in a square planar crystal field as it has only four nearby oxygen atoms and eventually adopts a low-spin state with zero magnetic moment (Fig. 6(c); see also
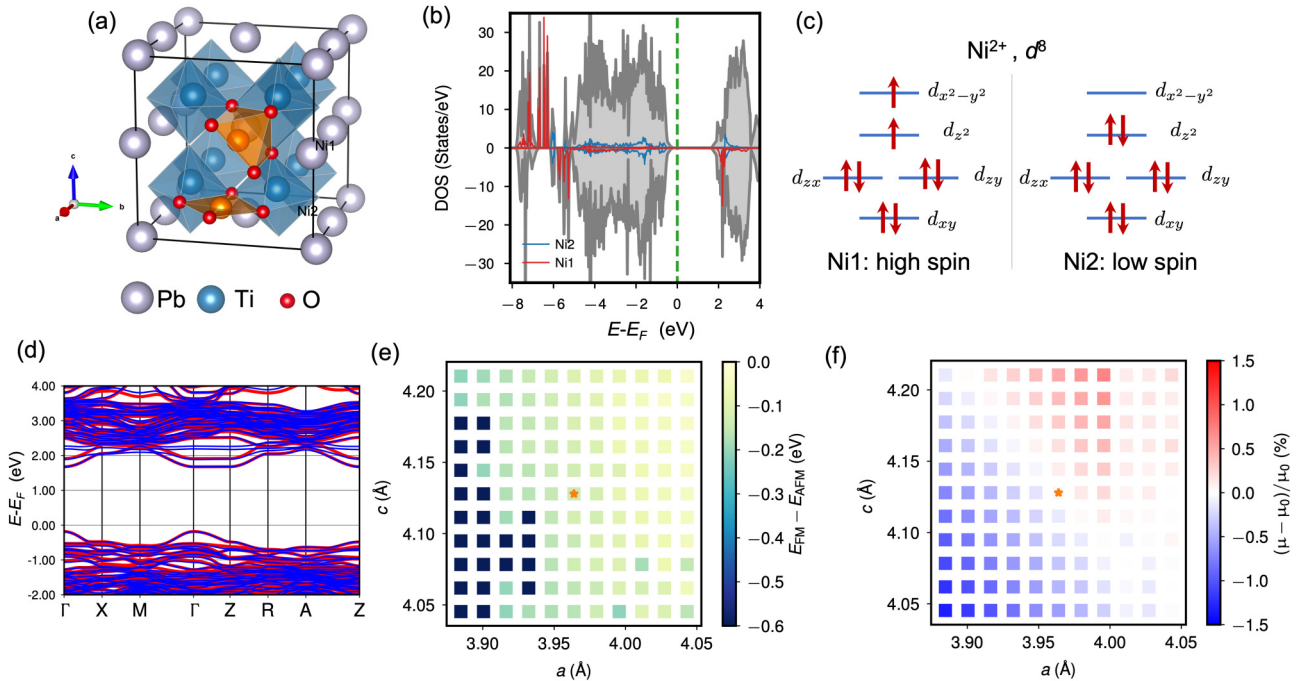

FIG. 6. (a) $2 \times 2 \times 2$ $PbTiO_3$ supercell with two $(Ni_{Pb})^\times$ defects. (b) Total density of states and the projected density of states of d orbital of two Ni atoms. (c) Schematics of crystal field splitting diagram for high-spin and low-spin states of Ni^{2+}. (d) Electronic band structure of Ni-doped $PbTiO_3$. Two-dimensional plot of (e) ferromagnetic-antiferromagnetic energy difference (ΔE) and (f) change in local magnetic moment of Ni atoms $(\mu - \mu_0)/\mu_0$ as a function of tetragonal lattice parameters.

the Supplemental Material [36] for the projected density of states of d orbitals of Ni atoms). It is noted that this magnetic state is 0.21 eV lower than the antiferromagnetic state where both Ni atoms are spin polarized, which may explain the very large magnetic Curie temperature observed experimentally. We propose that the presence of a mixed high-spin and low-spin states of Ni^{2+} in Ni-doped $PbTiO_3$ is responsible for the magnetization.

We further explore the effects of strain on the ferromagnetic-antiferromagnetic energy difference ($\Delta E = E_{FM} - E_{AFM}$) and the local magnetic moments on Ni atoms. As shown in the two-dimensional map of ΔE as a function of tetragonal lattice parameters (a, c), the magnetic state has lower energy for all strain conditions explored. We also quantify the effects of microscopic strain on the magnitude of magnetization by mapping out $(\mu - \mu_0)/\mu_0$ vs (a, c), where μ is the local magnetic moment of Ni and $\mu_0 = 1.68 \, \mu_B$ is the value calculated with experimental lattice constants. It is found that a few percent change in magnetization can be realized by modulating strain. All the optimized structures and energetics along with the projected density of states of d orbitals are presented in the Supplemental Material, S5–S10 [36]. Our first-principles investigations suggest the $(Ni_{Pb})^{\times}$ defect is likely to be responsible for the experimental ME coupling in Ni-doped PZT. The requirement of $(Ni_{Pb})^{\times}$ for magnetization also explains the relatively low magnetization observed experimentally as the majority of Ni dopants tend to replace B-site cations.

IV. CONCLUSIONS

PZTNi exhibiting tetragonal crystal structure and $P4mm$ symmetry was successfully synthesized for possible RT non-volatile multistate memory elements and for spintronics devices operated and controlled under external electric and magnetic fields. PZTNi exhibits ferromagnetism and ferroelectric ordering temperature well above RT with similar transition temperatures. PZTNi possesses low leakage current, large polarization, and weak ferromagnetism with a high ME coupling coefficient of $\sim$11.7 mV cm^{-1} Oe^{-1} (at $H_{ac} = 1$ Oe, $f = 1$ kHz) revealing a strong coupling between magnetic and electrical order parameters. The strong ME coupling above RT makes it a possible future alternative of other multiferroics with a strong possibility for applications in novel devices.

[1] W. Eerenstein, N. Mathur, and J. F. Scott, Nature **442**, 759 (2006).

[2] M. Fiebig, J. Phys. D: Appl. Phys. **38**, R123 (2005).

[3] J. Scott, Nat. Mater. **6**, 256 (2007).

[4] M. Bibes and A. Barthélémy, Nat. Mater. **7**, 425 (2008).

[5] L. Martin, Y.-H. Chu, and R. Ramesh, Mater. Sci. Eng., R **68**, 89 (2010).

[6] M. M. Waldrop, Nat. News **530**, 144 (2016).

[7] N. A. Hill, J. Phys. Chem. B **104**, 6694 (2000).

[8] N. A. Spaldin, S.-W. Cheong, and R. Ramesh, Phys. Today **63**(10), 38 (2010).

[9] G. Catalan and J. F. Scott, Adv. Mater. **21**, 2463 (2009).

[10] R. Palai, R. S. Katiyar, H. Schmid, P. Tissot, S. J. Clark, J. Robertson, S. A. T. Redfern, G. Catalan, and J. F. Scott, Phys. Rev. B **77**, 014110 (2008).

[11] D. M. Evans, M. Alexe, A. Schilling, A. Kumar, D. Sanchez, N. Ortega, R. S. Katiyar, J. F. Scott, and J. M. Gregg, Adv. Mater. **27**, 6068 (2015).

[12] S. Kumari, D. K. Pradhan, N. Ortega, K. Pradhan, C. DeVreugd, G. Srinivasan, A. Kumar, T. R. Paudel, E. Y. Tsymbal, A. M. Bumstead, J. F. Scott, and R. S. Katiyar, Phys. Rev. B **95**, 214109 (2017).

[13] Y. Li, Z. Wang, J. Yao, T. Yang, Z. Wang, J.-M. Hu, C. Chen, R. Sun, Z. Tian, and J. Li, Nat. Commun. **6**, 6680 (2015).

[14] J. Ma, J. Hu, Z. Li, and C. W. Nan, Adv. Mater. **23**, 1062 (2011).

[15] Y. Wang, J. Hu, Y. Lin, and C.-W. Nan, NPG Asia Mater. **2**, 61 (2010).

[16] D. K. Pradhan, V. S. Puli, S. Kumari, S. Sahoo, P. T. Das, K. Pradhan, D. K. Pradhan, J. F. Scott, and R. S. Katiyar, J. Phys. Chem. C **120**, 1936 (2016).

[17] C.-W. Nan, M. Bichurin, S. Dong, D. Viehland, and G. Srinivasan, J. Appl. Phys. **103**, 031101 (2008).

[18] D. K. Pradhan, S. Kumari, V. S. Puli, D. K. Pradhan, A. Kumar, S. V. Kalinin, R. K. Vasudevan, R. S. Katiyar, and P. D. Rack, J. Mater. Chem. C **8**, 12113 (2020).

[19] D. K. Pradhan, S. Kumari, and P. D. Rack, Nanomaterials **10**, 2072 (2020).

[20] S. Fusil, V. Garcia, A. Barthélémy, and M. Bibes, Annu. Rev. Mater. Res. **44**, 91 (2014).

[21] S. Kumari, D. K. Pradhan, R. S. Katiyar, and A. Kumar, in *Magnetic, Ferroelectric, and Multiferroic Metal Oxides* (Elsevier, Amsterdam, 2018), p. 571.

[22] S. Manipatruni, D. E. Nikonov, C.-C. Lin, T. A. Gosavi, H. Liu, B. Prasad, Y.-L. Huang, E. Bonturim, R. Ramesh, and I. A. Young, Nature (London) **565**, 35 (2018).

[23] S. Kumari, N. Ortega, A. Kumar, J. Scott, and R. Katiyar, AIP Adv. **4**, 037101 (2014).

[24] S. Kumari, N. Ortega, D. K. Pradhan, A. Kumar, J. F. Scott, and R. S. Katiyar, J. Appl. Phys. **118**, 184103 (2015).

[25] B. Legendre and M. Sghaier, J. Therm. Anal. Calorim. **105**, 141 (2011).

[26] M. Li, L. Xu, K. Shi, J. Zhang, X. Chen, Z. Hu, X. Dong, and J. Chu, J. Phys. D: Appl. Phys. **49**, 275305 (2016).

[27] F. Cordero, F. Trequattrini, F. Craciun, and C. Galassi, J. Phys.: Condens. Matter **23**, 415901 (2011).

[28] P. Giannozzi, S. Baroni, N. Bonini, M. Calandra, R. Car, C. Cavazzoni, D. Ceresoli, G. L. Chiarotti, M. Cococcioni, and I. Dabo, J. Phys.: Condens. Matter **21**, 395502 (2009).

[29] K. F. Garrity, J. W. Bennett, K. M. Rabe, and D. Vanderbilt, Comput. Mater. Sci. **81**, 446 (2014).

[30] V. I. Anisimov, J. Zaanen, and O. K. Andersen, Phys. Rev. B **44**, 943 (1991).

[31] M. Cococcioni and S. de Gironcoli, Phys. Rev. B **71**, 035105 (2005).

[32] J. Rodríguez-Carvajal, Physica B (Amsterdam, Neth.) **192**, 55 (1993).

[33] J. Joseph, T. Vimala, V. Sivasubramanian, and V. Murthy, J. Mater. Sci. **35**, 1571 (2000).

[34] P. Roy-Chowdhury and S. B. Deshpande, J. Mater. Sci. **22**, 2209 (1987).

[35] A. Sani, M. Hanfland, and D. Levy, J. Phys.: Condens. Matter **14**, 10601 (2002).

[36] See Supplemental Material at http://link.aps.org/supplemental/10.1103/PhysRevB.104.174415 for further details of SEM, EDS, STEM, DSC, J-V, XPS, and DFT results.

[37] D. K. Pradhan, P. Misra, V. S. Puli, S. Sahoo, D. K. Pradhan, and R. S. Katiyar, J. Appl. Phys. **115**, 243904 (2014).

[38] K. Abe, N. Sakai, J. Takahashi, H. Itoh, N. Adachi, and T. Ota, Jpn. J. Appl. Phys. **49**, 09MB01 (2010).

[39] M. Rahaman, T. Imai, T. Sakamoto, S. Tsukada, and S. Kojima, Sci. Rep. **6**, 1 (2016).

[40] M. M. Rahaman, T. Imai, T. Sakamoto, M. Al Helal, S. Tsukada, and S. Kojima, J. Alloys Compd. **735**, 1063 (2018).

[41] J. Toulouse, F. Jiang, O. Svitelskiy, W. Chen, and Z.-G. Ye, Phys. Rev. B **72**, 184106 (2005).

[42] J. Frantti, Y. Fujioka, A. Puretzky, Y. Xie, Z.-G. Ye, and A. Glazer, J. Appl. Phys. **113**, 174104 (2013).

[43] A. G. Souza Filho, K. C. V. Lima, A. P. Ayala, I. Guedes, P. T. C. Freire, F. E. A. Melo, J. Mendes Filho, E. B. Araújo, and J. A. Eiras, Phys. Rev. B **66**, 132107 (2002).

[44] M. Fontana, A. Ridah, G. Kugel, and C. Carabatos-Nedelec, J. Phys. C Solid State Phys. **21**, 5853 (1988).

[45] D. K. Pradhan, S. Sahoo, S. K. Barik, V. S. Puli, P. Misra, and R. S. Katiyar, J. Appl. Phys. **115**, 194105 (2014).

[46] H. Nakayama and H. Katayama-Yoshida, Jpn. J. Appl. Phys. **40**, L1355 (2001).

[47] G. M. Keith, M. J. Rampling, K. Sarma, N. M. Alford, and D. Sinclair, J. Eur. Ceram. Soc. **24**, 1721 (2004).

[48] G. Srinivasan, E. T. Rasmussen, J. Gallegos, R. Srinivasan, Y. I. Bokhan, and V. M. Laletin, Phys. Rev. B **64**, 214408 (2001).

[49] V. Naik and R. Mahendiran, Solid State Commun. **149**, 754 (2009).

[50] S. Kumari, N. Ortega, A. Kumar, S. Pavunny, J. Hubbard, C. Rinaldi, G. Srinivasan, J. Scott, and R. S. Katiyar, J. Appl. Phys. **117**, 114102 (2015).

[51] E. Jartych, T. Pikula, K. Kowal, J. Dzik, P. Guzdek, and D. Czekaj, Nanoscale Res. Lett. **11**, 234 (2016).

[52] C. M. Fernández-Posada, A. Castro, J.-M. Kiat, F. Porcher, O. Peña, M. Algueró, and H. Amorín, Nat. Commun. **7**, 12772 (2016).

[53] K. Zhai, D. S. Shang, Y. S. Chai, G. Li, J. W. Cai, B. G. Shen, and Y. Sun, Adv. Funct. Mater. **28**, 1705771 (2018).

[54] J. Coey, M. Venkatesan, and C. Fitzgerald, Nat. Mater. **4**, 173 (2005).